Solid state recycling of aluminium chips: Multi-technique characterization and analysis of oxidation

Mathilde Laurent-Brocq, Lola Lilensten, Clémence Pinot, André Schulze, Amandine Duchaussoy, Julie Bourgon, Eric Leroy, A. Erman Tekkaya

Laurent-Brocq, M., et al., *Solid state recycling of aluminium chips: Multi-technique characterization and analysis of oxidation.* Materialia, 2023. **31**: p. 101864. https://doi.org/10.1016/j.mtla.2023.101864

Solid state recycling of aluminium chips: multi-technique characterization and analysis of oxidation

Mathilde Laurent-Brocq[1], Lola Lilensten[2], Clémence Pinot[1,2], André Schulze[3], Amandine Duchaussoy[4], Julie Bourgon[1], Eric Leroy[1], A. Erman Tekkaya[3]

[1] Univ. Paris-Est Créteil, CNRS, ICMPE, UMR7182, F-94320 Thiais, France

[2] PSL University, Chimie ParisTech, CNRS, Institut de Recherche de Chimie Paris, Paris, France 75005

[3] Institute of Forming Technology and Lightweight Components, TU Dortmund University, 44227 Dortmund, Germany

[4] Groupe de physique des matériaux, UMR CNRS 6634, Normandie Université, Avenue de l'université, 76800, Saint Etienne du Rouvray, France

Corresponding author :

Mathilde Laurent-Brocq

mathilde.laurent-brocq@cnrs.fr

UMR 7182 CNRS Université Paris-Est Créteil

2, rue Henri Dunant (bât D) - 94320 Thiais

+33 (0)1 56 70 30 65

Abstract

Solid-state recycling of metallic alloys is a promising alternative method which avoids remelting and reduces significantly the CO_2-emission compared to remelting. Contamination being critical for solid-state recycling, the objective of this study is to quantify and localize oxygen contamination at each step of the process. Pre-compacted AA6060 aluminium alloy machining chips were hot-extruded. The oxygen intake and the formation of oxides were quantified and localized through a multi-technique characterization, including X-ray photoelectron spectroscopy and transmission electron microscopy. The overall oxygen content is found to increase at every step of the recycling process. Analyses reveal that the initial thin Al_2O_3 layer on the chips gets covered by a MgO layer during pre-annealing and hot extrusion. Thus, alloying elements, as Mg, are involved in oxidation. It results in a tenfold increase of the oxygen content in the extrudate accompanied by a complex network of oxides with an average thickness of 290 nm and a low density. Thus, tuning processing parameters is a promising leverage to limit oxidation and improve chip welding, which will probably depend on the alloying elements.

Keywords

Solid-state recycling, extrusion, microstructural characterization, aluminium alloy, X-ray photoelectron spectroscopy, transmission electron microscopy.

1. Introduction

In order to cut down CO_2 emissions, recycling of aluminium alloys is of utmost relevance. Indeed, by saving metal extraction from mines, and avoiding the energy required to reduce aluminium ores to metal, large energy and CO_2 savings can be reached [1]. Considering the large amount of aluminium used, the savings are substantial. However, further improvements can be achieved. Indeed, recycling is classically done through remelting of the material, which is energy costly – although in a smaller extent than primary production of metal but still in order of primary production of steel – and induces losses of material through oxidation or evaporation, or primary aluminium consumption for dilution [2, 3]. An alternative approach considers the solid-state recycling of metallic chips, based on the direct mechanical processing of chips with severe plastic deformation, mostly using extrusion [4, 5]. This approach takes advantage, among others, of the wide use of the established extrusion in aluminium alloys processing [6]. By avoiding the remelting step, the energy consumption is reduced by a factor of 3 to 4 compared to conventional recycling [3, 7].

Although other processing approaches have been proposed for solid state recycling, such as high-pressure torsion [7], screw extrusion [8], friction stir extrusion [9] and spark plasma sintering [10], they do not allow to process such large quantities of materials, compared to classical extrusion. Solid state recycling of aluminium by extrusion has therefore been the favored approach so far. It consists in the compaction of chips, and the subsequent extrusion of the compacted ingot. The strong shear produced in the material during the process has been shown to help consolidating the chips [11]. Initially proposed by Stern in 1945 [12], this recycling approach has been subjected to an increasing number of studies in the recent years, for chips of aluminium alloys, but also of other metals and alloys such as magnesium or titanium alloys or Al-based composite materials [5, 11, 13-18]. However, by introducing external elements, and in spite of some promising results, the recyclability of composite materials might be reduced, compared to recycling of metallic chips of a single composition.

To obtain profiles from recycled material that can compare to profiles from cast billets, the welding quality of chips has long been identified as a key parameter [5, 19]. In aluminium alloys, an oxide layer is formed initially at the chip surface, due to its interaction with the environment. The layer gets incorporated in the material during extrusion, but might be broken down due to the shear and surface expansion during extrusion, allowing free chip surfaces to weld. Improvements of the welding have therefore been sought, by tuning and carefully optimizing the processing parameters. Among the relevant parameters, the extrusion ratio and the die design (flat face, porthole or ECAP dies) have been shown to play a tremendous role in the formation of quality extrudates [13-15]. A numerical model initially used to characterize the welding of parts to assemble has also been adapted for the chip extrusion. It takes into account the die type and extrusion processing parameters, and was validated experimentally with the chip extrusion of AA6060 alloy, hence allowing predicting the welding of the chips during hot extrusion [20-22]. Fully dense semi-finished profiles were produced and exhibited very promising mechanical properties. A chip-based profile obtained with a flat-face die has an ultimate tensile strength which represents 75 % of the value of a reference material processed using an initial cast ingot and nearly 95% if processed by an ECAP-die [23]. For a profile which was subsequently rolled and annealed, it goes up to 97 % of the properties of the reference material, processed with the same steps [24].

Although it is well known that oxygen reacts with aluminium to form an oxide layer at the surface of the material, the details of the oxide layer at the chip surface, and what it becomes after extrusion, have not

been investigated from an experimental point of view. This has been identified as one of the scientific bottleneck to overcome [17]. Once incorporated into the extrudate, the oxides will remain in the alloy. Contrary to re-melting, solid-state recycling does not permit any removal of contamination. A better understanding of the formation and nature of the oxide layer could help tune numerical models, and improve the process by increasing chip welding. The objective of the present paper is therefore to quantify and localize the oxygen contamination at each step of the solid-state recycling process. To fulfill this aim, the chip extrusion of AA6060 is considered, as this material already benefits from several studies [14, 21, 24], and its processing is therefore mastered. A detailed characterization of the oxygen intake is provided using a multi-technique approach.

2. Experimental

For the experimental tryouts to produce chip-based profiles, aluminium alloy AA6060 was processed in the following consecutive steps: (a) production of chips by turning, (b) compaction of the chips to chip-based billets, (c) homogenization of the chip-based billets and (d) hot extrusion of the chip-based billets to round solid profiles. Those steps are represented on Fig. 1 and are detailed below.

Table 1 : Chemical composition of the AA6060 aluminium alloy, as measured by optical emission spectroscopy

	Si	Fe	Cu	Mn	Mg	Cr	Zn	Ti	Others	Al
wt. %	0.44	0.21	0.02	0.05	0.39	0.00	0.011	0.01	0.01	98.86
at. %	0.42	0.10	0.009	0.02	0.42	0.00	0.005	0.006	0.005	99.00

AA6060 cast bars were supplied by apt Hiller GmbH. The chemical composition was measured by optical emission spectroscopy (Table 1). The sample coming from the cast bar was named AA-cast. In the first step, the casting skin of those as-received cast bars was turned off and sorted out. Afterwards the chips were produced by longitudinal turning without lubrication to prevent a contamination of the chips (Fig. 1a). The parameters were set to a cutting speed v_c = 400 m/min, a feed of f = 0.5 mm and a cutting depth of a_p = 2.25 mm to achieve homogenous chips with equal dimensions. After turning the average hardness of the chips was 79 HV0.2. Those chips were named AA-chips. For better handling, the chips were compacted to chip-based billets with a hydraulic press applying a constant compaction force of 500 kN, without lubrication, in a steel tube with an inner diameter of 60 mm (Fig. 1b). The resulting chip-based billet was a cylinder with a diameter of 60 mm, a length of 92 mm and a relative density ρ of 2,15 g/cm^3 which is 80% of the density of cast aluminium (ρ = 2.7 g/cm^3).

To release the severe plastic deformation induced by machining and cold compaction and to dissolve Mg_2Si hardening precipitates if any, the chip-based billets were homogenized prior to extrusion (Fig. 1c). The billets were heated to T_{Billet} = 550 °C and held at this temperature for six hours in an electric furnace with standard atmospheric conditions. The chips homogenized in the same conditions as the compacted chip-based billet were named AA-chips-H.

The extrusion experiments were carried out on a direct extrusion press (Collin Technology GmbH), which has a maximum extrusion force of 2.5 MN (Fig. 1d). A simple flat-face die was used to extrude a solid cylindrical profile geometry with a diameter of d = 12 mm (Fig. 1e). The container diameter of the extrusion press amounts to 66 mm, resulting in an extrusion ratio R = 30.25. The extrusion parameters were chosen as follows: billet temperature T_{Billet} = 550 °C, die and container temperature T_{Die} = 450 °C and ram speed

v_{Ram} = 2 mm/s. Those parameters were selected based on previous studies and should ensure a sound welding of the chips during the process and a homogenous material flow inside the die. After extrusion the profiles were cooled in ambient air. Their appearance was satisfying (i.e.: no delamination or any other defects such as air bubbles were visible). Samples cut from this chip-based profile were named AA-chips-HE.

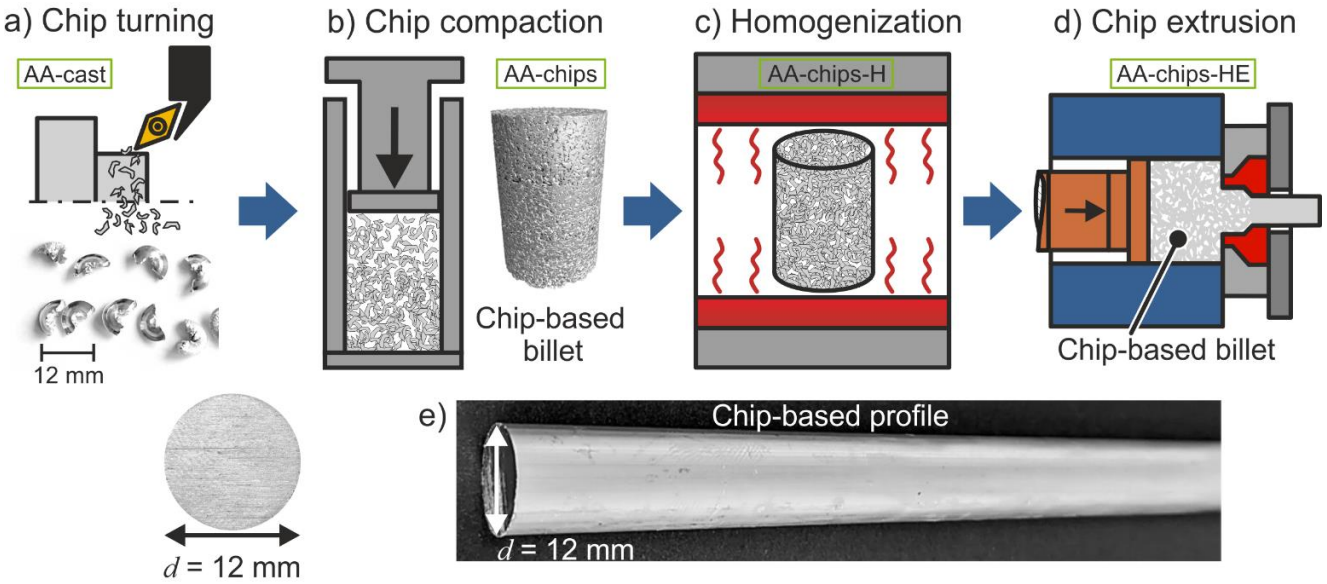

Fig. 1 : Process steps for chips extrusion (a,b,c and d) to obtain an extruded chip-based profile (e). For (a) to (d), a scheme of the process is depicted and the name of the corresponding sample is indicated. A photo of the sample is also given for (a), (b) and (e).

All samples were characterized by Reducing Melting InfraRed absorption (RMIR) to determine the average content of O. For each sample, a mass between 2.2 and 2.5 g was analyzed.

The surface layer on the chips (i.e., AA-chips and AA-chips-H) was characterized by X-ray Photoelectron Spectroscopy (XPS) using a Thermo Scientific K-Alpha XPS instrument with a monochromatized Al X-ray source (1486.6 eV). The take-off angle was 90° and the diameter of the analyzed area was 400 µm. High resolution spectra of the C 1s, Al 2p, O 1s, Mg 2p and Si 2p were collected with a pass energy of 50 eV and a step size of 0.1 eV. The surface was etched by an Ar ion beam at an energy of 1000 eV for duration of 10 s. Composition and thickness were calculated after this first etching. When needed to further study the evolution in the depth, the ion beam energy was increased up to 4000 eV while the duration was 60 s. Data processing were performed with Avantage, the Thermo Electron software. The binding energy of each peak was corrected by the amount required to shift the metal Al 2p peak at its reference value (ie: 73 eV, [25]). A Shirley correction was made for the background.

The chip-based extrudate (AA-chips-HE) was characterized by Electron Probe MicroAnalysis (EPMA). X-Ray maps were acquired with a CAMECA SX100 EPMA. Analyzing crystals used were: LPC1 (synthetic multilayer, $2d_{hkl}$=6 nm) for O Ka, TAP (Thallium Acid Phthalate crystal, $2d_{hkl}$=2.545 nm) for Mg Ka, Si Ka, and Al Ka and LIF (Lithium Fluoride, 2_{dhkl}=0.4027 nm). The experimental conditions were the following: acceleration voltage of 15kV, beam current of 100nA, time per pixel of 30ms. The maps were acquired in stage movement mode, that means that the beam was static, and the sample was moving. To be able to characterize submicrometric oxides with a low density, the spot size was 0.6 µm for a total area of 1228.8 x 1228.8 µm² (Fig. 6). Two additional maps with a spot size of 1 µm were recorded on a total area of respectively 1024 x 1024 µm² (Fig. S 2) and of 512 x 512 µm² (Fig. S 3)

AA-chips-HE was also characterized by Transmission Electron Microscopy (TEM). Here, round 3mm large TEM samples were prepared until 100 µm thickness and then electropolished at -30 °C (243 K) using a twin jet system in solution composed of 66.6 % methanol and 33.3 % Nitic acid at a voltage of 12 V. TEM observations

were performed on a Tecnai F20 ST operating at 200 kV equipped with an edax detector system (60 mm² windowless). On bright field images, the oxide layer thickness was measured in more than 15 locations. Energy Dispersive Xray Spectroscopy (EDS) was used in scanning mode to identify the chemical composition of sub-micrometric precipitates. The composition of 19 precipitates was determined after excluding the signal of Al, which originates from the matrix, and of C, which is likely to be due to surface contamination. Then, for each type of precipitates, an average composition was calculated.

Finally, AA-chips-HE and, for comparison, the starting aluminium ingot AA-cast were characterized by Atom Probe Tomography. APT analyzes were carried out using a CAMECA LEAP-4000HR instrument. APT tips were prepared using electro-polishing (electrolyte: 98 % $C_8H_{16}O_3$ + 2 % $HClO_4$). Samples were field evaporated at 40 K in ultra-high vacuum (10^{-11} mbar) with electric pulses (pulse fraction of 20 %, repetition rate 200 kHz) at a detection rate of 0.2 %. Data processing was performed with IVAS and Gpm3dSoft software. In order to detect the presence of clusters and to estimate their size, composition and volume fraction, the Isoposition method (IPM) was applied [26]. In this method, a composition is attributed to each atom in function of its environment (neighboring atoms), and a compositional threshold can then be defined to determine which atoms are considered to belong to a cluster and which are part of the matrix. In order to identify precipitates, it is then necessary to define a maximum distance below which the atoms will belong to the same precipitate and a minimum number of atoms below which the atoms will be considered as belonging to the matrix. In this study, a composition threshold of 2.7 at.% of Mg was set with D_{max} of 0.5 nm and N_{min} of 10 atoms.

3. Results

First, the average oxygen content was measured in each sample by RMIR (Fig. 2). For the starting aluminium ingot (AA-cast), the oxygen concentration is below the detection limit of the technique (<0.001 wt. %). In machining chips (AA-chips), an oxygen content of 0.002 +/- 0.0002 wt. % (i.e.: 20 ppm) was detected, which is still very low. Afterwards, at each step of the solid-state recycling process, the oxygen content increases: it is of 0.009 +/- 0.001 wt. % after the homogenization treatment (AA-chips-H) and it goes up to 0.022 +/- 0.001 wt. % after extrusion (AA-chips-HE). It is recalled that the oxygen present in the chips is incorporated in the extrudate. Here the measurements indicate that there is an additional oxygen intake during heat treatment and extrusion. This was expected given the fact that those two steps are performed under atmospheric conditions. Since the solubility limit of O in Al is extremely low [27], formation of oxides is expected.

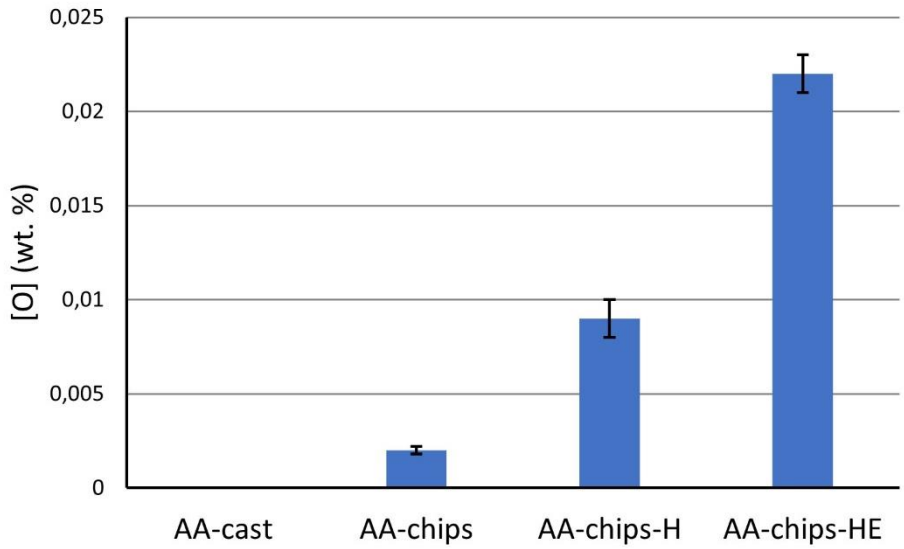

Fig. 2 : Evolution of oxygen average concentration at each step of the process, as measured by RMIR. (Material: AA 6060)

Secondly, an XPS surface analysis, which typically probes depths of 2 to 3 nm, was performed with the objective of following the evolution of the native oxide of the cast sample during machining and homogenization. To begin, AA-cast and AA-chips were studied.

Their XPS spectra are plotted on Fig. 3 and Fig. S 1. They are very similar and thus the same peak fittings were applied. The C 1s spectrum was simply fitted by two peaks, one for carbon-carbon bonds and the other for carbon - oxygen bonds. Two peaks can be clearly distinguished on the Al 2p spectrum: the one at the lowest binding energy corresponds to a metallic bond (Al_{met}) while the other one corresponds to an oxide bond (Al_{ox}). Although the photo-electrons had to penetrate through the surface oxide layer, the metallic bond peak is apparent, which indicates that this oxide layer is very thin. Mg 2p and Si 2p, whose concentration is only of few atomic percent, were fitted respectively by a single peak and by a metal and oxide peak. Finally, the O1s spectrum exhibits a large peak, which is very likely the result of the convolution of several peaks. It was chosen not to decompose it but rather to analyze the composition ratio to determine the nature of the oxide layer.

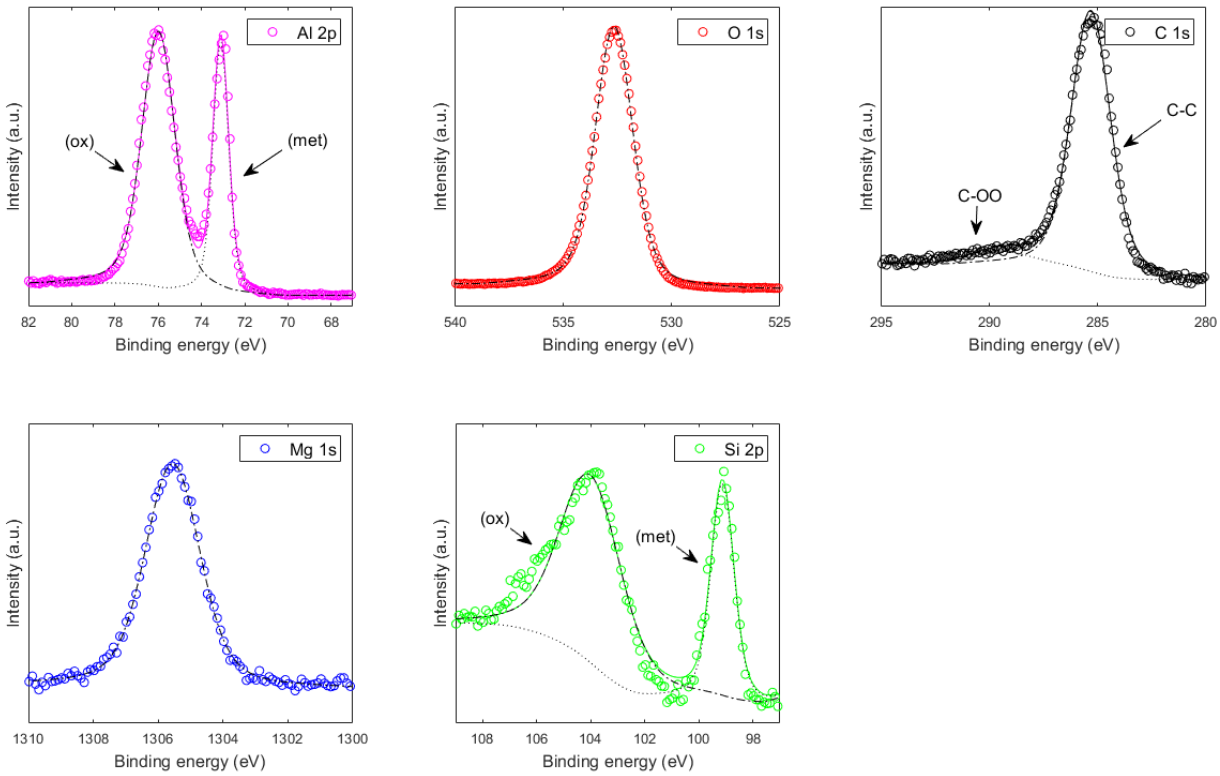

Fig. 3 : XPS spectra of machined chips (AA-chips). The colored circles and black dashed lines correspond respectively to the experimental spectra and peak fitting. For Al 2p, C1s and Si 2p, the spectrum is fitted by two peaks, the corresponding bonds are indicated and the total fit is plotted as a color straight line.

The compositions calculated from the fitting described above are given in Table 2. For AA-cast and AA-chips, the most concentrated elements are Al and O. Moreover, the aluminium over oxygen concentration ratio is of 0.5 and 0.6 respectively for AA-cast and AA-chips, which is compatible with the stoichiometry of the aluminium oxide Al_2O_3 ([Al]/[O]=0.66) but not with the hydroxide $Al(OH)_3$ (([Al]/[O]=0.33). For a deeper analysis, it was supposed that oxygen was involved in Al_2O_3 and also interacted with the other alloying elements, hence involved in MgO, SiO_2 and in C-OO bonds. The corresponding ratio $\frac{\sum x_i M_i}{O} = \frac{3/2 \cdot [Al_{ox}] + [Mg] + 2 \cdot [Si_{ox}] + 2 \cdot [C_{C-OO}]}{O}$ was calculated. A value of 1.0 was obtained, which is in very good agreement with the initial assumption. Thus, the oxide layer of AA-chips is composed of 90 % of Al_2O_3, 7 % of SiO_2 and 3 % of MgO. Carbon is considered to be part of an adsorbed contamination layer. For AA-cast, results are similar, with slightly more SiO_2.

To calculate the thickness of the oxide layer, the presence of SiO_2 and MgO was neglected and a mono-layer model was used [28]. Then the thickness d of Al_2O_3 can be expressed as:

$$d = \lambda_{Al}^{Al_2O_3} * \sin(\theta) * \ln\left(1 + \frac{\lambda_{Al}^{pure\ Al}}{\lambda_{Al}^{Al_2O_3}} * \frac{D_{Al}^{pure\ Al}}{D_{Al}^{Al_2O_3}} * \frac{I_{Al,ox}}{I_{Al,met}}\right) \qquad \text{Eq. (1)}$$

Where λ_X^Y is the inelastic mean free path (IMFP) of element X in the phase Y, θ is the take-off angle of the analyzed electron, θ=90° in this work, D_X^Y is the number density of X in Y, $I_{Al,ox}$ and $I_{Al,met}$ are the peak areas deduced from the Al 2p spectrum. The used material data are given in Table S 1. A thickness of 7 and 4 nm were calculated respectively for AA-cast and AA-chips. This is in good agreement with data from the literature for a native oxide for pure Al [25] or for aluminium alloy [29]. Moreover, the XPS analysis of AA-cast and AA-

chips provide qualitatively and quantitatively similar results. It indicates that, despite the fact that AA-chips surface is not flat, results are reliable.

Table 2 : XPS analysis of cast alloy (AA-cast), machined chips (AA-chips) and homogenized chips (AA-chips-H). The surface layer composition, obtained from deconvoluted high resolution spectra, is given.
Concentration ratios are calculated: the major metal (i.e.: Al or Mg) over oxygen; weighted metals and carbon over oxygen (ie: $\frac{\sum x_i M_i}{O} = \frac{3/2\cdot[Al_{ox}]+[Mg]+2\cdot[Si]+2\cdot[C_{ox}]}{O}$. The thickness d of the oxide layer is also given (aluminium oxide for AA-cast and AA-chips; superposed magnesium and aluminium oxides for AA-chips-H).

Sample name	Composition (% at.)							[Metal]/[O] ratio			d (nm)
	Al_{met}	Al_{ox}	Mg	Si_{ox}	O	C_{C-C}	C_{C-OO}	Al_{ox}/O	Mg/O	$\sum x_i M_i / O$	
AA- cast	4.1	28	0.3	3.3	53	10	1.1	0,5	-	1,0	7
AA-chips	11	25	1.2	1.7	42	16	1.4	0,6	-	1,0	4
AA-chips-H	1.8	2.7	33	0	39	20	2.4	-	0,9	1,1	20

Then, the chips after the homogenization treatment (AA-chips-H) were characterized by XPS. The spectra and the corresponding compositions are given respectively on Fig. 4 and in Table 2. The main difference is the significantly larger content of magnesium which increases from 1.2 at. % in AA-chips to 33 at. % in AA-chips-H. There is a concomitant decrease of Al and Si, which is not detected at all. It is mentioned that the O 1s spectrum was fitted with two peaks which were used only to determine the total content of oxygen and were not attributed to specific bondings.

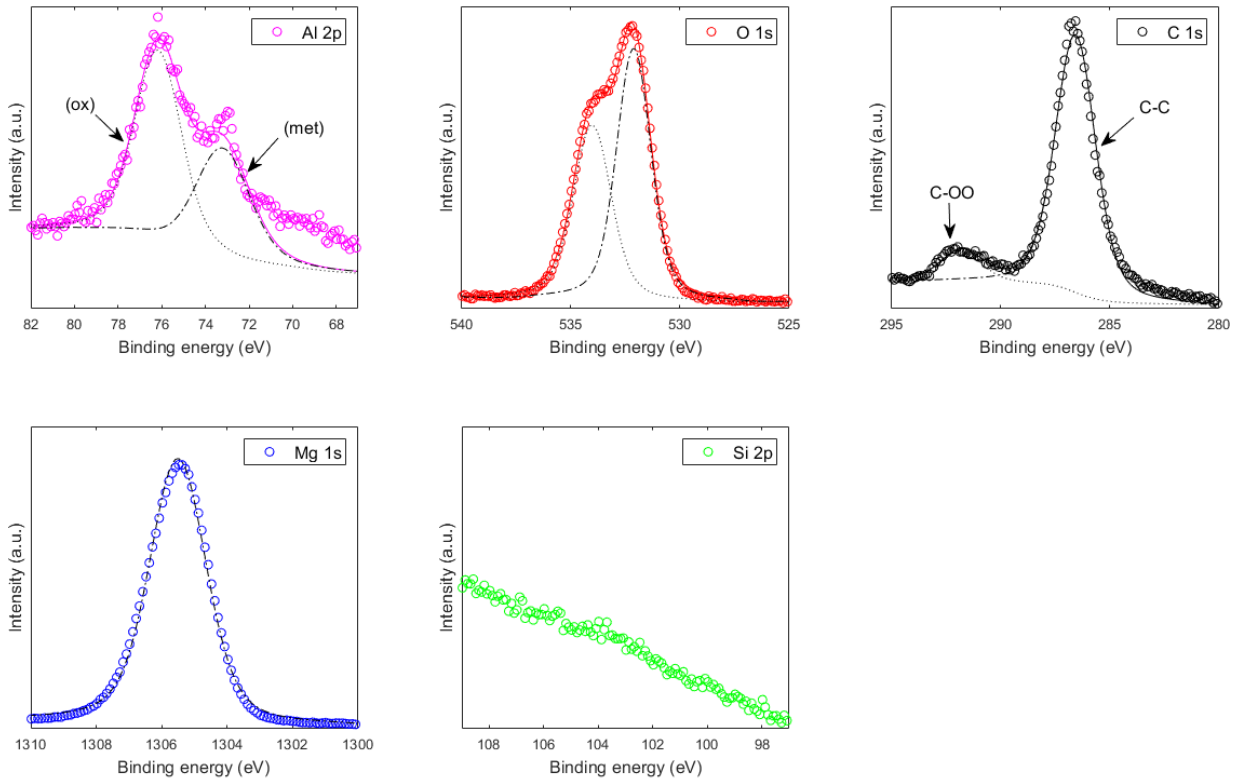

Fig. 4 : XPS spectra of chips after the homogenization treatment (AA-chips-H). The colored circles and black dashed lines correspond respectively to the experimental spectra and peak fitting. For Al 2p, O 1s and C 1s, the spectrum is fitted by two peaks, the corresponding bonds are indicated and the total fit is plotted as a color straight line. There is no peak on the Si 2p spectrum, thus there is no fitting.

The magnesium over oxygen ratio is of 0.9. This is slightly smaller than the stoichiometry of the magnesium oxide MgO and clearly larger than the one of the hydroxide $Mg(OH)_2$. Thus, it can be assumed that oxygen is involved in MgO and, as previously, in Al_2O_3 and C-OO bonds. The corresponding ratio is of 1.1, indicating a slight depletion of oxygen compared to this assumption but an overall satisfying agreement. Next, to clarify the organization of this mixed oxide layer, further sputtering and XPS analysis were performed. The deduced in-depth concentration profile is plotted on Fig. 5. Along with sputtering, the magnesium content decreases while the one of Al oxide peak increases. It indicates that MgO is the outer layer while Al_2O_3 is the inner one. A slight content of Si(ox) appears at the fourth sputtering level. This is probably the thin SiO_2 layer detected on the machined chips AA-chips.

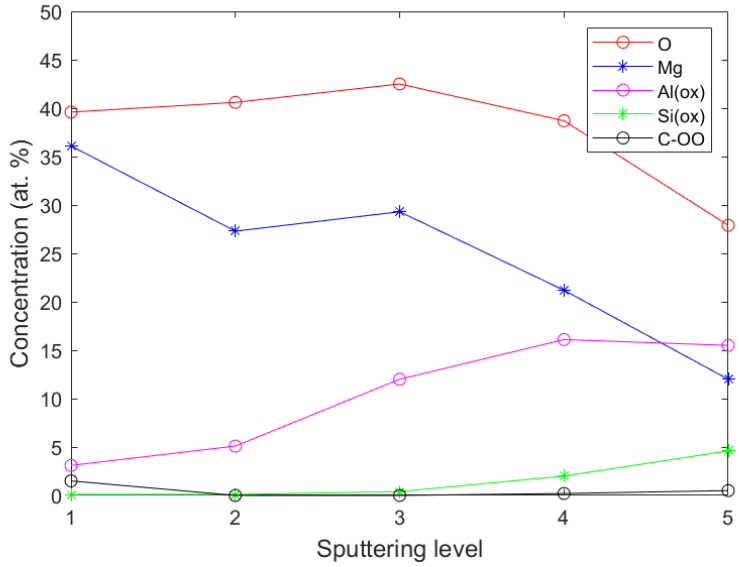

Fig. 5 : XPS in-depth concentration profile of chips after the homogenization treatment (AA-chips-H). Only the elements involved in bondings with oxygen are plotted.

Here, to calculate the thickness, the presence of SiO_2 is again neglected and a two-layer model is used [28]. The layers are assumed to be homogeneous and continuous (i.e.: covering the whole surface). First, the peak areas of Mg, Al(ox) and Al(met) are expressed:

$$I_{Mg} = K * A(\theta) * \sigma_{Mg} * \lambda_{Mg}^{MgO} * T_{Mg} * D_{Mg}^{MgO} * sin(\theta) * \left[1 - exp\left(-\frac{d_1}{\lambda_{Mg}^{MgO} * sin(\theta)}\right)\right] \quad \text{Eq. (2)}$$

$$I_{Al,ox} = K * A(\theta) * \sigma_{Al} * \lambda_{Al}^{Al2O3} * T_{Al} * D_{Al}^{Al2O3} * sin(\theta) * \left[1 - exp\left(-\frac{d_2}{\lambda_{Al}^{Al2O3} * sin(\theta)}\right)\right] * exp\left(-\frac{d_1}{\lambda_{Al}^{MgO} * sin\,(\theta)}\right) \quad \text{Eq. (3)}$$

$$I_{Al,met} = K * A(\theta) * \sigma_{Al} * \lambda_{Al}^{pure\ Al} * T_{Al} * D_{Al}^{pure\ Al} * sin(\theta) * exp\left(-\frac{d_2}{\lambda_{Al}^{Al2O3} * sin(\theta)}\right) * exp\left(-\frac{d_1}{\lambda_{Al}^{MgO} * \sin(\theta)}\right) \quad \text{Eq. (4)}$$

Where K is a constant specific to the XPS apparatus, σ_X and T_x are respectively the cross-section of photo-ionization and the transmission factor of element X, d1 and d2 are the thickness of respectively the outer

MgO layer and the inner Al_2O_3 layer. By combining Eq. (2) and Eq. (3) with Eq. (4), the thickness d_1 and d_2 can be expressed as:

$$d_1 = \lambda_{Al}^{MgO} * sin(\theta) * ln\,[1 + exp\left(-\frac{d_2}{\lambda_{Al}^{Al2O3} * sin(\theta)}\right) * \frac{\sigma(Al)}{\sigma(Mg)} * \frac{T_{Al}}{T_{Mg}} * \frac{\lambda_{Al}^{pure\ Al}}{\lambda_{Mg}^{MgO}} * \frac{D_{Al}^{pure\ Al}}{D_{Mg}^{MgO}} * \frac{I_{Mg}}{I_{Al,met}}] \quad \text{Eq. (5)}$$

$$d_2 = \lambda_{Al}^{Al2O3} * sin(\theta) * ln\,(1 + \frac{\lambda_{Al}^{pure\ Al}}{\lambda_{Al}^{Al2O3}} * \frac{D_{Al}^{pure\ Al}}{D_{Al}^{Al2O3}} * \frac{I_{Al,ox}}{I_{Al,met}}) \quad \text{Eq. (6)}$$

Since the Al(met) peak is already detected before in-depth sputtering (Fig. 4), the thickness was calculated using those spectra, which guarantees that the whole oxide layer is taken into account. The used material data are given in Table S 1. Values of 16 nm and 4 nm were calculated for respectively the MgO and Al_2O_3 layer, resulting in a total oxide thickness d of 20 nm. The thickness of the Al_2O_3 layer is similar to the one measured on AA-chips.

Thus, the homogenization treatment on chips induced a significant growth of an outer MgO layer on top of the already existing Al_2O_3 layer. First, it should be recalled that, according to an Ellingham diagram, MgO is more stable than Al_2O_3 [30]. Now, kinetics should also be taken into consideration. At room temperature, a nanometric amorphous Al_2O_3 layer is formed in few minutes on the clean surface of a metal and protects it [31]. In the case of a Mg containing alloy, a very thin inner MgO layer appears too [32]. This corresponds to the situation of the AA-cast and AA-chips samples. When the temperature increases, the Al_2O_3 oxide crystallizes and becomes porous, allowing the diffusion of Mg towards the surface and the formation of an outer MgO layer [31, 32]. The transition temperature for Al_2O_3 crystallization decreases when the Mg content increases. For a 3003 Al alloys, containing 0.03 wt. % of Mg, it is around 520°C to around 370°C [33]. Since the Mg content of the studied A6060 alloy (i.e., 0.39 wt. %) is larger than the 3003 Al alloy, its transition temperature should be even lower. Thus, the homogenization treatment at 550°C is expected to be far above the crystallization transition, which is in agreement with the observed outer MgO oxide. To summarize, the nature of the observed oxide layers on AA-cast, AA-chips and AA-chips-H is in agreement with the literature.

Thus, the observed increase of the average oxygen content due to the homogenization treatment (Fig. 2) is due to the oxidation of magnesium and not of aluminium. In other words, the alloying elements are involved.

The chip oxide layer is embedded within the extrudate during extrusion. The next step is thus to characterize the bulk of AA-chips-HE. First, it was done at the micron scale by EPMA. Preliminary characterizations show that oxides were submicronic and with a low density. Thus, a mosaic of maps was recorded and reconstructed to be able to characterize a large area yet with a high spatial resolution (more details in section 2). Fig. 6 displays oxygen and magnesium EPMA maps in the middle of the extrudate cylinder. A complex network of lines enriched simultaneously in Mg and O is observed. Based on XPS results, those magnesium oxides are very likely to be the oxides that were on the chips. They will be called Prior Chips Boundaries (PCB), in reference to the term Prior Particle Boundaries (PPB) which is commonly used in powder metallurgy.

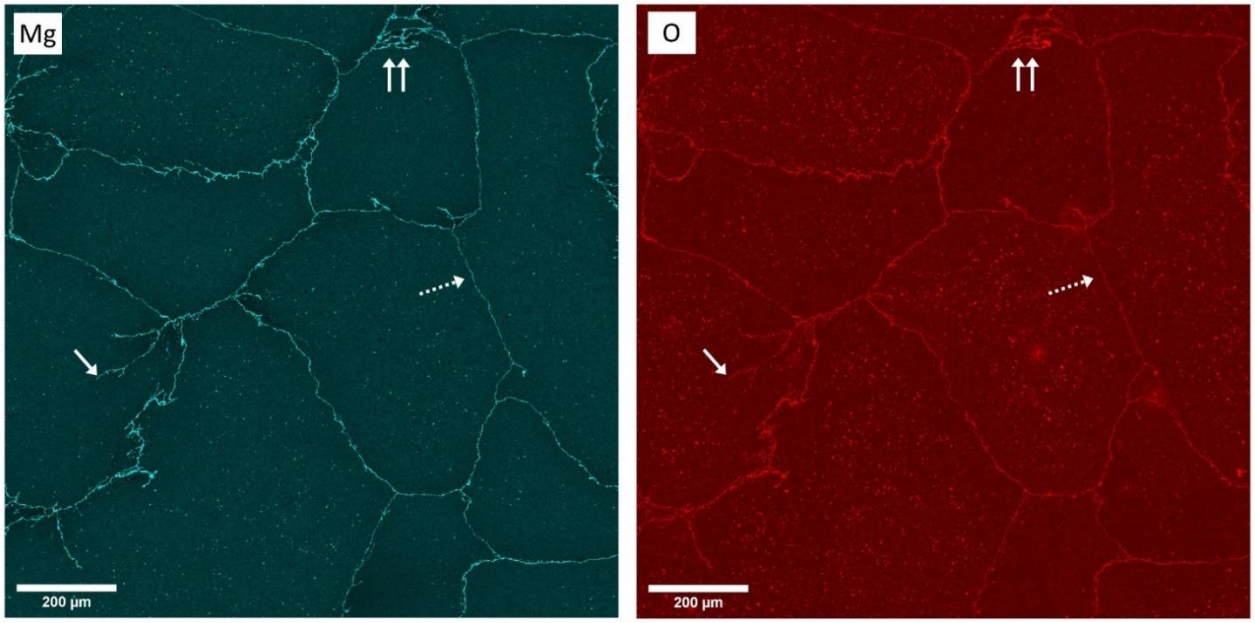

Fig. 6 : Mg and O elemental maps obtained by EPMA of the solid-state recycled aluminium alloy (AA-chips-HE). The observed area is perpendicular to the extrusion direction and close from the middle of the extrudate cylinder. Dashed and straight arrows indicate respectively continuous and interrupted Prior Chips Boundaries.

The network of PCB is composed of straight as well as irregular and interrupted lines (respectively dashed and straight arrows on Fig. 6). Some few areas contain a higher density of PCB (double white arrows on Fig. 6). The PCB delimit domain with an approximate length of 300 to 600 µm. The diameter of chips being around 8 mm, the ratio of chip over PCB size is of 13 to 27, which is comparable to the applied extrusion ratio of 30. This complex network of PCB illustrates the fact that chips, and as a consequence the oxide layer on top of them, were strongly deformed during extrusion. But oxides are still present, they are neither finely nor homogeneously distributed. At the periphery of the cylinder (Fig. S 2), the PCB domains are smaller and more elongated. Lines are more frequently interrupted. This reveals a macroscale heterogeneity of deformation during extrusion.

On a smaller area (Fig. S 3), Al, Si and Fe were also mapped. None of them appear to be enriched at the PCB. Aluminium oxides were detected in the chip oxide layer by XPS. Al being the matrix (i.e.: the major element), it is very difficult to detect concentration variation of this element. At that point, the presence of aluminium oxides at the PCB cannot be excluded.

The thickness of PCB is also of interest. Since it is of the same order of magnitude than the EPMA resolution, another characterization technique is needed. This is why Transmission Electron Microscopy was used. Lines of precipitates can be observed on bright field images of Fig. 7a and Fig. S 4. According to EDS maps (Fig. 7b), those precipitates are enriched in oxygen and magnesium, among other things. Thus, they correspond to the oxides at the PCB previously observed by EPMA. Here again, some line interruptions are observed (black arrows on Fig. 7a). Thanks to the higher magnification offered by TEM, it can also be noticed that the thickness of the lines varies greatly: from 85 to 750 nm, with an average of 290 nm. This is dramatically larger than the oxide layer thickness that was measured on homogenized chips by XPS. It confirms that oxidation continues during extrusion, which was already highlighted by RMIR measurements. Moreover, a few discontinuities within the lines can be detected (red arrows on Fig. 7a). It could mean that, at some places, the chip oxide layer was broken, despite its ongoing growth. This would be in favor of true welding of chips during extrusion. Cracks, which would be indication of poor welding, were not noticed around the oxides.

EDS maps give more insight on the oxides' composition: qualitatively and semi-quantitatively (Fig. 7b and Fig. S 5b). Indeed, parts of the lines are simultaneously enriched in Mg and O (white arrows on Fig. 7b), with a

ratio corresponding to MgO. This is in agreement with qualitative EPMA characterization. Areas enriched with Mg, Si and O are also present (dashed white arrows on Fig. 7b). The measured composition is $(Si_5,Mg)O_2$, which could be the SiO_2 oxide with some substitution of Si by Mg. However, if MgO and SiO_2 oxides of few nanometers were next to each other, it could probably not be sorted out. It is underlined that the presence of silicon at the PCB was not detected by EPMA, probably because it is less concentrated than Mg. In addition to oxides, some copper sulfides were observed scarcely on the PCB. Their shape is oval, with a large diameter of around 1 µm, and their composition corresponds to Cu_2S. It means that some contaminations tend to agglomerate on PCB. Finally, some Fe_2Si precipitates were frequently observed outside the PCB (they were also visible by EPMA). Those precipitates are common yet unwanted in aluminium alloys. A depletion of aluminium is observed at the PCB and the areas of oxygen enrichment are always combined with a Mg or Si presence. So, the presence of aluminium oxides larger than few hundreds of nanometers is very unlikely. Nevertheless, the presence of very thin aluminium oxides intricated with Mg and Si oxides remain possible.

It means that, during extrusion, no significant aluminium oxide growth takes place and that the increase of oxidation is due to magnesium and possibly silicon oxidation. How the thin aluminium oxide inner layer of homogenized chips evolves during extrusion is not known for now. This consumption of magnesium to form oxides could modify its average concentration in the matrix (ie: far from the PCB), which could lead to an alteration of the precipitation hardening.

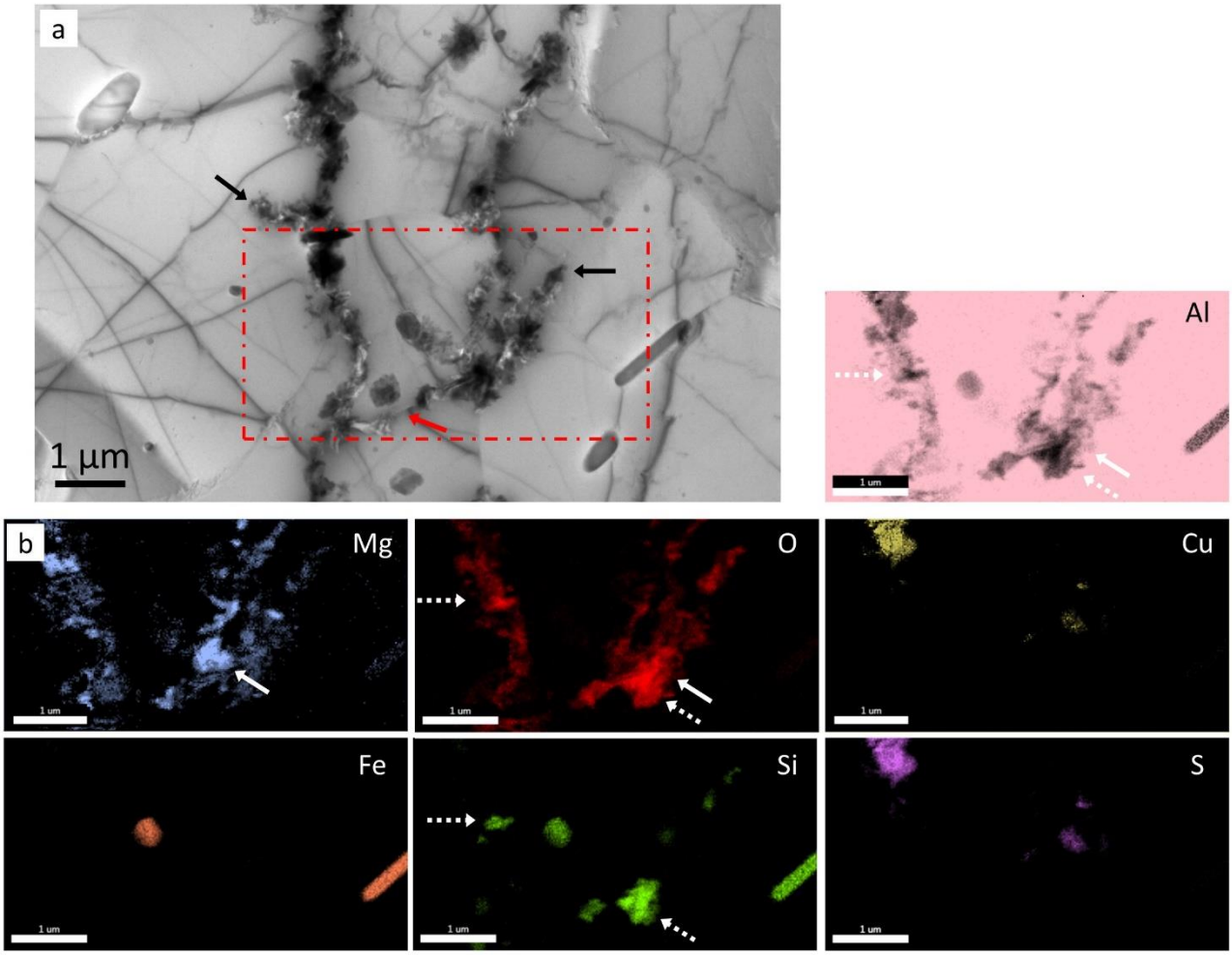

Fig. 7 : TEM characterization of the solid-state recycled aluminium alloy (AA-chips-HE). (a) Bright field image. Black and red arrows indicate respectively interrupted oxide lines and discontinuities within those lines. (b) EDS mapping of the area from (a) delimited by the dashed red rectangle. The scale bar is of 1 µm for all images. White straight and dashed arrows indicate respectively magnesium and silicium oxide.

Finally, APT analyses were performed on the chips-based extrudate (AA-chips-HE) and, for comparison, on the starting cast material (AA-cast). The 3D reconstruction of volumes (Fig. 8) shows the distribution of Mg and Si ions. In the AA-cast volume, calculations based on the mass spectrum indicate that there is 0.326 at. % of Mg (Table 3). For AA-chips-HE, using the same peak identification in the mass spectrum than for the AA-cast sample, the Mg content varies from 0.279 to 0.339 at. %, depending on the analyzed volume (Table 3). Thus, there is no detectable depletion of Mg in AA-chips-HE, which can be explained by the low density of the PCB and of the Mg oxides which precipitate along them. Nevertheless, the Mg distribution may be more heterogenous. It is mentioned that both samples have a slightly lower Mg concentration compared to the measured macroscopic concentration of 0.42 at. % (Table 1).

Now the dispersion of solute atoms can be considered at a near atomic scale (Fig. 8a and b). In AA-cast, Mg and Si are homogeneously dispersed in the matrix with, however, some visible clusters. In the volume 1 of the chips-based extrudate material, similar repartition of ions is observed. Al-Si-Mg alloys typically exhibit precipitates (GP-zones) in naturally aged samples [34-36], so such APT results are expected. To detect and characterize them more precisely, the Isoposition method was used (section 2). Fig. 8c shows the presence of clusters enriched in Mg and Si, typically GP-zones which are formed after natural ageing, common for this material. This is confirmed by the size and the concentration of Mg and Si of these clusters (Table 3), which are close to values from the literature [34-36]. The density of these clusters is lower for AA-chips-HE than for AA-cast but, more importantly, their distribution appears less homogeneous. Indeed, in the three volumes analyzed for AA-chips-HE, the measured densities are 69, 33 and 1.6 clusters/μm^3. However, this difference in density of clusters have only little influence on the Mg content in the matrix for volume 1 and 2. For volume 3, the content is lower. This could indicate that volume 3 is close to a prior chip boundary, which induces a depletion in Mg that has diffused out to the chip boundary and oxidized.

To conclude, formation of MgO precipitates at PCB does not impact the content of Mg solutes in the matrix (i.e.: far away from the PCB). The size and the composition of GP-zones are not affected either. Nevertheless, it may induce some composition heterogeneity, which especially affects the GP-zone density.

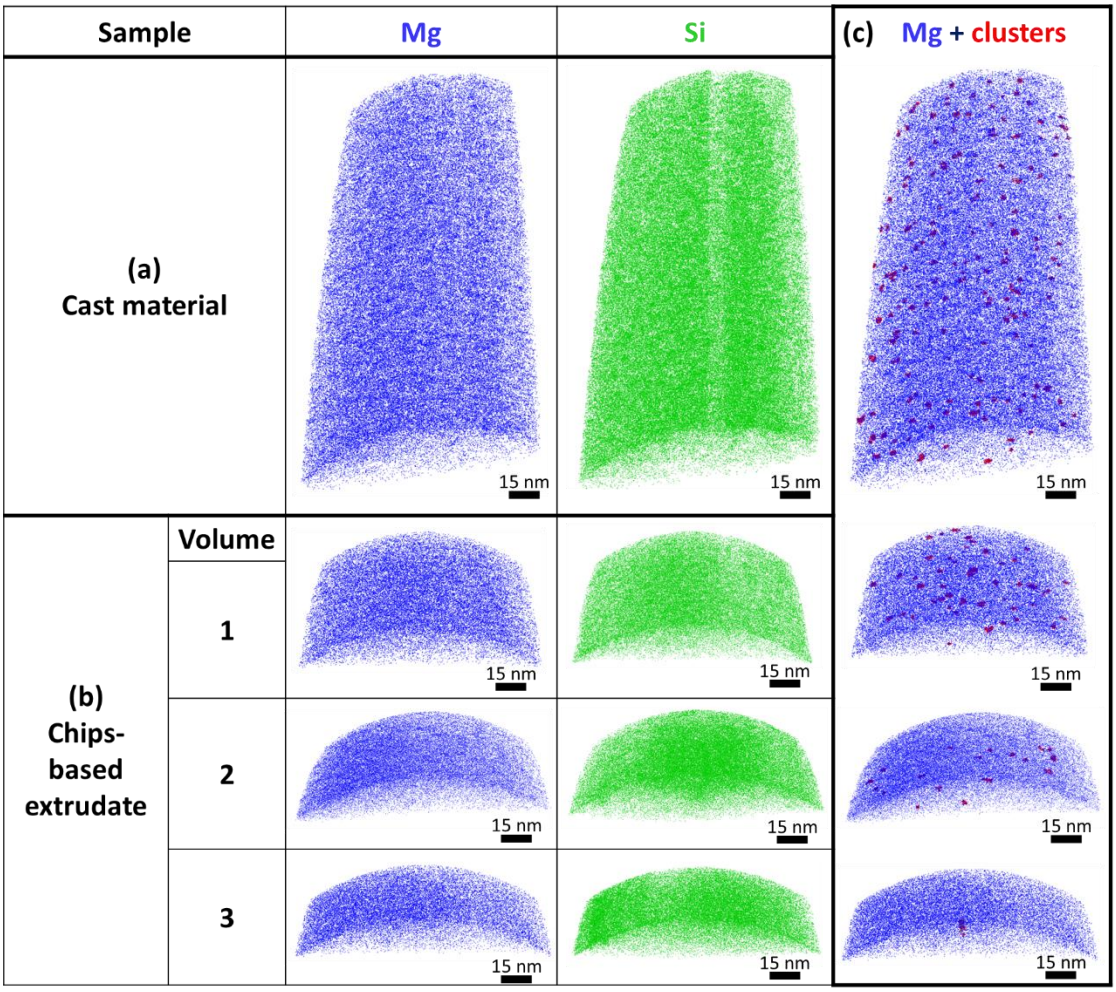

Fig. 8 : 3D reconstruction of volumes analyzed by APT of (a) cast material (AA-cast), (b) chips-based extrudate material (AA-chips-HE) for Mg, Si ions and (c) Mg clusters determined by iso-position method.

Table 3 : APT measurements of composition of Mg in the matrix, of Mg and Si in the clusters, of the clusters average radius and density for cast and chips-based extrudate samples.

Sample name	[Mg] in matrix (at. %)		[Mg] in clusters (at. %)		[Si] in clusters (at. %)		Clusters radius (nm)		Clusters density (μm^{-3})
AA-cast	0.326	±0.002	4.74	±0.67	2.15	±1.14	1.22	±0.14	103
AA-chips-HE area 1	0.339	±0.003	4.66	±0.55	3.03	±1.30	1.26	±0.15	69
AA-chips-HE area 2	0.336	±0.003	4.67	±0.57	2.45	±2.00	1.25	±0.17	33
AA-chips-HE area 3	0.279	±0.004	4.83	(only one)	7.43	(only one)	1.18	(only one)	1.6

4. Discussion

Characterization of oxygen in a metallic alloy is often complex because, oxygen being a light element, it is not precisely measured by most of the techniques. Moreover, there is always an oxygen contamination (from the atmosphere or polishing products for instance), which can be difficult to sort out from the oxygen actually inside the material. Here, oxygen content is low (from 0.002 to 0.022 wt. %), oxide layers on chips are nanometric, oxides in extrudates are submicrometric and of low density, which increases the characterization challenge.

We use a set of techniques to determine various parameters: RMIR for average oxygen content, XPS for composition and thickness of oxide layer on chips, EPMA for localization of oxides in extrudates, TEM for their size and composition, APT for the matrix composition. All those results were already shown to be in qualitative agreement and to permit to quantify and/or localize oxygen. Now, we will combine the obtained results to calculate additional parameters related to oxygen and go further in the description of the oxidation during the solid-state recycling process. The calculations and the data are detailed in Supplementary Material.

The average mass oxygen content $[O]_{wt}$, as measured by RMIR in all samples, can be expressed as:

$$[O]_{wt} = \frac{\rho_{ox} \cdot f_{O,ox} \cdot e_{ox} \cdot S_{ox}}{\rho_{Al} \cdot V_{Al}} \qquad \text{Eq. (7)}$$

Where ρ, e, S and V are respectively the density, the thickness, the surface and the volume, 'ox' and 'Al' subscripts refer respectively to oxide and aluminium alloy, $f_{O,ox}$ is the molar fraction of oxygen in the oxide.

Thanks to XPS analysis, the nature of oxides for cast and chips samples is known (ie: Al_2O_3 and/or MgO). The Al_2O_3 and MgO density ρ_{ox} and fraction of oxygen in the oxide $f_{O,ox}$ are known. The thickness of the oxide layer e_{ox} was also determined thanks to XPS. Based on all those experimental data and on Eq. (7), the surface-to-volume ratio S_{ox}/V_{Al} can be calculated. This ratio is indeed complicated to estimate by geometrical considerations, due to complex shape and rough surface of the chips. Using the experimental data, S_{ox}/V_{Al} of 0.6, 7.3 and 8.2 mm^{-1} are calculated respectively for AA-cast, AA-chips and AA-chips-H. It comes as no surprise that machining chips has dramatically increased the surface-to-volume ratio. It is mentioned that the AA-cast is a small 1 cm^3 cube. For a standard cast ingot (length of around 8 cm, diameter of 6 cm), the surface-to-volume ratio would be even smaller (0.09 mm^{-1}). It is also underlined that, considering the uncertainty on both oxygen content and oxide thickness measurements, surface-to-volume ratio of both chip samples can be considered as equal, which is consistent with the fact that the chips' geometry remains the same during homogenization annealing.

Assuming a constant S_{ox}/V_{Al} ratio between the chips before and after homogenization, and to overcome the uncertainty on this term, the ratio $[O]_{wt,\,Ch\text{-}H}/[O]_{wt,\,Ch}$ can also be calculated using the experimental data and Eq. (7). A value of 4.05 is found, close to the 4.5 value obtained using the values provided by RMIR, confirming the reliability of XPS measurements and of the chosen approach.

During extrusion, the oxide layer on the chips is incorporated within the extrudate. TEM characterization has shown that the oxides within the AA-chips-HE are larger than the oxide layer on homogenized chips characterized by XPS (respectively 290 and 20 nm). We can make the hypothesis that, during extrusion, chips oxide layer grows up to 290 nm and, knowing the previously calculated surface-to-volume ratio of chips and using Eq. (7), an oxygen content of 0.1 wt. % is calculated. This value is five times larger than the actual measured oxygen content in AA-chips-HE (ie: 0.022 wt. %). Thus, the hypothesis of a homogenous growth of the oxide on the whole surface of chips during extrusion can be rejected. This is in agreement with TEM images of AA-chips-HE, on which discontinuous lines of oxides were observed. Instead, two extreme options

can be proposed. The first one suggests that only a fraction of the chip oxide layer grows during extrusion. Based on Eq. (7), on the oxygen content and oxide thickness measured respectively by RMIR and TEM in AA-chips-HE and on the surface-to-volume ratio of chips previously calculated, a fraction of around 20 % is calculated. The second one suggests that the surface to volume ratio of chips increases during extrusion due to the high local extrusion strain (surface expansion), creating new clean metal surfaces where oxides grew. The previous approach cannot sort out those two mechanisms, and a combination of both end cases can actually be obtained.

The significant enhancement of oxide growth during extrusion appears surprising at first. Indeed, extrusion is performed at the same temperature than the previous homogenization treatment (i.e., 550°C) and lasts only few minutes, compared to 6h of homogenization. This could be due to a local temperature increase of the extrudate or to an influence of plastic deformation. The oxide layer on homogenized chips could also have a more complex morphology than the homogeneity and continuity assumed for calculating its thickness, which would lead to a misestimation. This will be studied in more detail in the future.

Finally, the in-depth characterization proposed above is summarized into an oxidation mechanism in Fig. 9. The initial ingot, with very low surface-to-volume ratio, is made of AA 6060, covered with a 7 nm thick native Al_2O_3 layer (Fig. 9a). After being turned into chips, the surface-to-volume ratio increases strongly. The chips are still covered with the native Al_2O_3 layer, with a thickness of 4 nm (Fig. 9b). It results in an increase of the total oxygen content. During homogenization at 550°C for 6 hours, the Al_2O_3 layer crystallizes, and becomes porous, allowing for Mg to diffuse out and form a 16nm-thick layer of MgO, leading to a more significant increase of oxygen content (Fig. 9c). The final step of extrusion is more complex to analyze. Indeed, according to the thin film theory [20], adapted for chip extrusion [21], the surface extension of the chips, which is induced by extrusion, cracks the oxide surface layer, exposing the metal. This new metal surface is immediately oxidized by the air trapped within the pre-compacted billet, creating a new oxide layer. The surface extension goes on, finally managing to break this newly formed oxide layer and to put into contact two clean metal surfaces. It results in a sound metal bounding. In agreement with this theory, the measured oxygen intake greatly increases during extrusion. Nevertheless, the measured oxides in extrudates are significantly larger than the oxide layer measured on homogenized chips, indicating that this layer may have pursued its growth during extrusion. Then, two end-scenarios (Fig. 9d1 and d3) are proposed, considering either a growth of oxides exclusively on the pre-existing layer, on about 20% of this surface (Fig. 9d1), or the formation of new oxides exclusively on new metal surfaces (Fig. 9d2). Note that the height of the new oxides in the schematic of Fig. 9 is not at scale, TEM measurement showed a thickness of about 290 nm. An intermediate scenario, depicted in Fig. 9d3, shows a combination of oxide growth on top of former MgO oxides and on fresh AA6060 surfaces. Oxides at the surfaces and the newly formed metal surfaces illustrated in Fig. 9d1 to d3 are incorporated in the extrudates. The incorporated oxides form the complex network of PCB, revealed by EPMA analyses (Fig. 6) and TEM analyses (Fig. 7). Although the oxides formed during extrusion, in green in Fig. 9, are mostly made of MgO, as indicated by EPMA analyses (Fig. 6), TEM have revealed that other compounds might be found there. Their average size of 290 nm is order of magnitude larger than the maximum oxide thickness of 3 nm, which allows welding of two aluminum surfaces [37]. In other words, a poor welding is anticipated around those oxides, although no cracks were observed. On the contrary, the newly formed metal surfaces allow local sound welding.

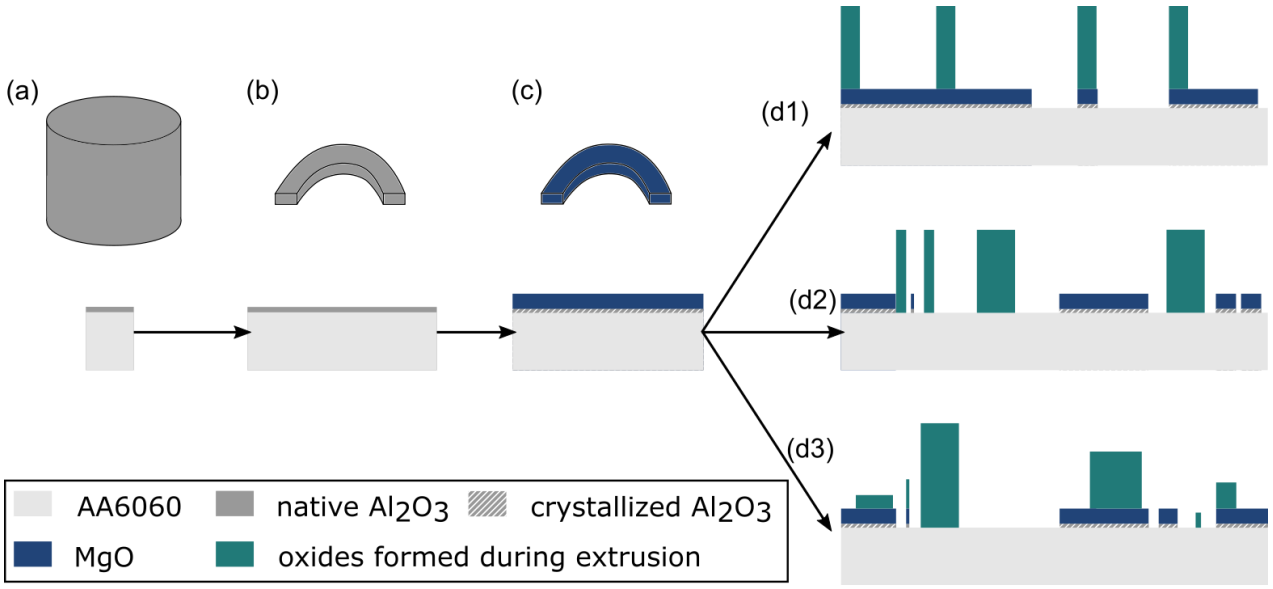

Fig. 9 : Oxidation mechanism during solid-state recycling: (a) initial ingot, low surface-to-volume ratio. (b) machined chips, high surface-to-volume ratio. (c) homogenized chips. (d1) to (d3): chips extension during extrusion and the possible scenario of breakage and growth of surface oxides. For (a) to (c), the global shape (above) and a cross-section (below) are depicted.

Hence, the results presented here provide an in-depth microstructural characterization of the oxidation, ultimately providing a schematical oxidation mechanism. Although some assumptions have been made, such as the constant thickness of the oxide, the results provide a good qualitative and reasonably quantitative characterization of the oxidation.

Based on this oxidation mechanism, some ways of improvement can be proposed. The most efficient way to limit oxidation is very likely to perform heat treatment and extrusion under an inert atmosphere. To be able to do so, the compacting could be replaced by cladding the chips within an inert atmosphere before heat treatment and extrusion. This approach is successfully performed in powder metallurgy processing routes [38]. Nevertheless, it would be a complex and costly procedure. To facilitate the industrialization of solid-state recycling, it is preferable to remain close from the processing steps already at use in the industry of cast-billet extrusion (i.e.: heat treatment and extrusion under atmospheric conditions [39]). A second way of improvement is to finely tune processing. Decreasing the temperature of both homogenization treatment and extrusion appears as a promising first step. To do so, a deep understanding of oxidation kinetics and its relationship with the processing parameters is required. This second way will probably be a better compromise to limit both oxidation and cost.

5. Conclusion

The oxygen contamination during solid-state recycling of a 6060 aluminium alloy was characterized. Samples from each step of the process were considered: the cast alloy as reference, the turning chips, the chips after the homogenization treatment and the extrudate obtained after hot extrusion. To be able to quantify and localize oxygen, a combination of techniques was used: RMIR for the average concentration, XPS for composition and thickness of surface layers, EPMA for global localization, TEM for local characterization and APT to measure the concentration of the matrix on a nanometric scale. The main results are the following:

- The average oxygen concentration increases at each step of the process, and especially during extrusion: It goes from 0.009 wt. % of O in the turning chips up to 0.022 wt. % in the chip-based extrudate.

- Chips are covered with a thin Al2O3 layer of 4 nm. During homogenization, due to the temperature increase, a thicker MgO layer grows on top of the Al_2O_3 layer. This is expected for aluminium alloys containing Mg.
- Those oxides are embedded within the bulk during extrusion. They form a complex network of lines, which are named Prior Chip Boundaries (PCB). They delimit domains of several hundreds of micrometers. PCB are made out mainly of oxides, but also of other intermetallics or precipitates, in a much smaller extent.
- Those oxides have an average thickness of 290 nm and are composed mainly of MgO with additional binary Mg and Si oxides.
- The average concentration of Mg in the matrix, far away from the PCB, remains unchanged but the distribution of Mg enriched GP-zones seems more heterogenous.

In conclusion, the main source of oxygen contamination is not the unavoidable Al_2O_3 oxides already present on the chips, but the additional oxidation during the process. Thus, tuning processing parameters appear as a strong leverage to limit oxidation and the subsequent properties degradation. The involvement of alloying elements in the oxidation, mainly Mg but also Si, should also be stressed. It means that, when applied to another aluminium alloys compositions, the oxidation during solid-state recycling could be drastically different. Thus, the generalization of solid-state recycling to a wide panel of aluminium alloy families will probably require significant adjustments of processing parameters.

In the future, the processing parameters, and in the first place the homogenization and extrusion temperature, will be made varied in order to decrease the oxidation and favor sound chip welding. The hardening precipitation in chip-based extrudates will also be studied to check whether this essential feature is modified or not compared to cast based aluminium alloys.

6. Acknowledgements

The authors thank Pierre Dubot for fruitful discussion on XPS data acquisition and analysis. French METSA platform is acknowledged for the APT allocation time.

7. Supplementary materials

7.1. Additional characterization

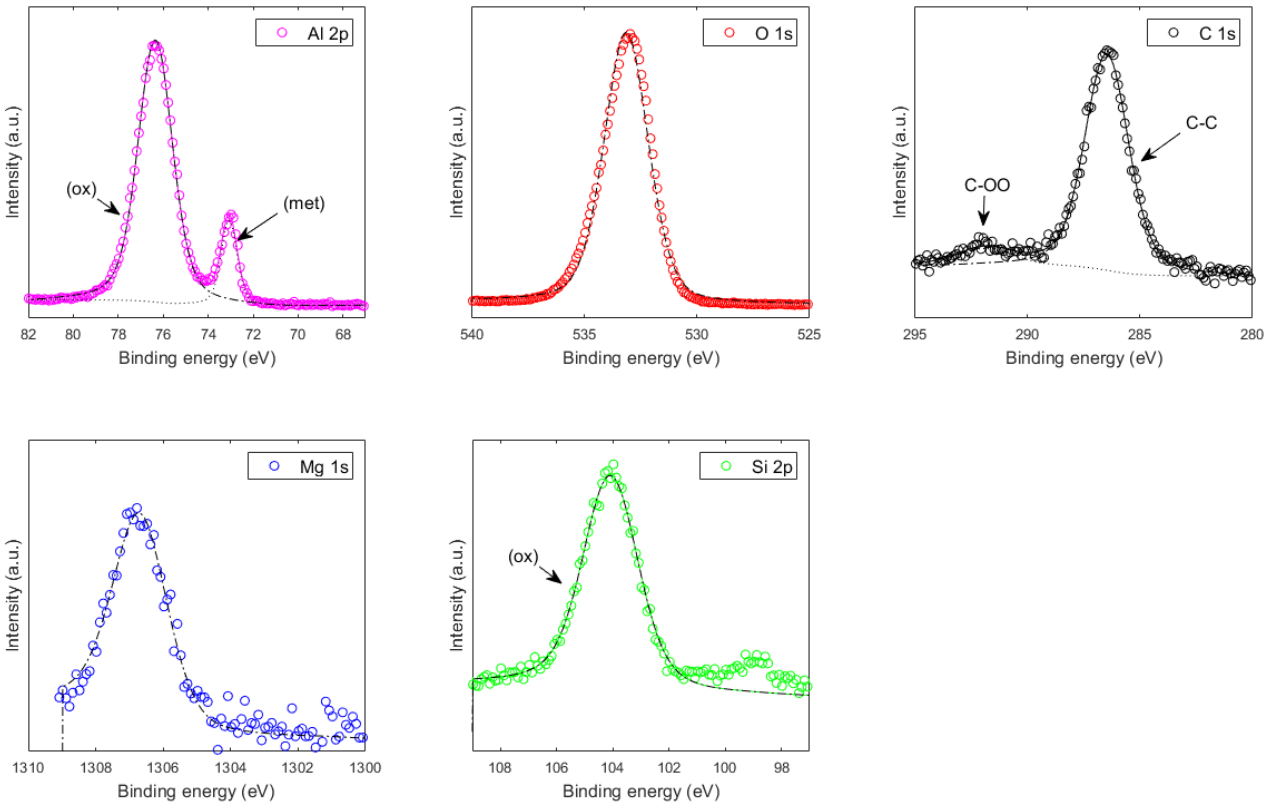

Fig. S 1 : XPS spectra of the starting aluminium ingot (AA-cast). The colored circles and black dashed lines correspond respectively to the experimental spectra and peak fitting. When the spectrum is fitted by two peaks, the corresponding bonds are indicated and the total fit is plotted as a color straight line.

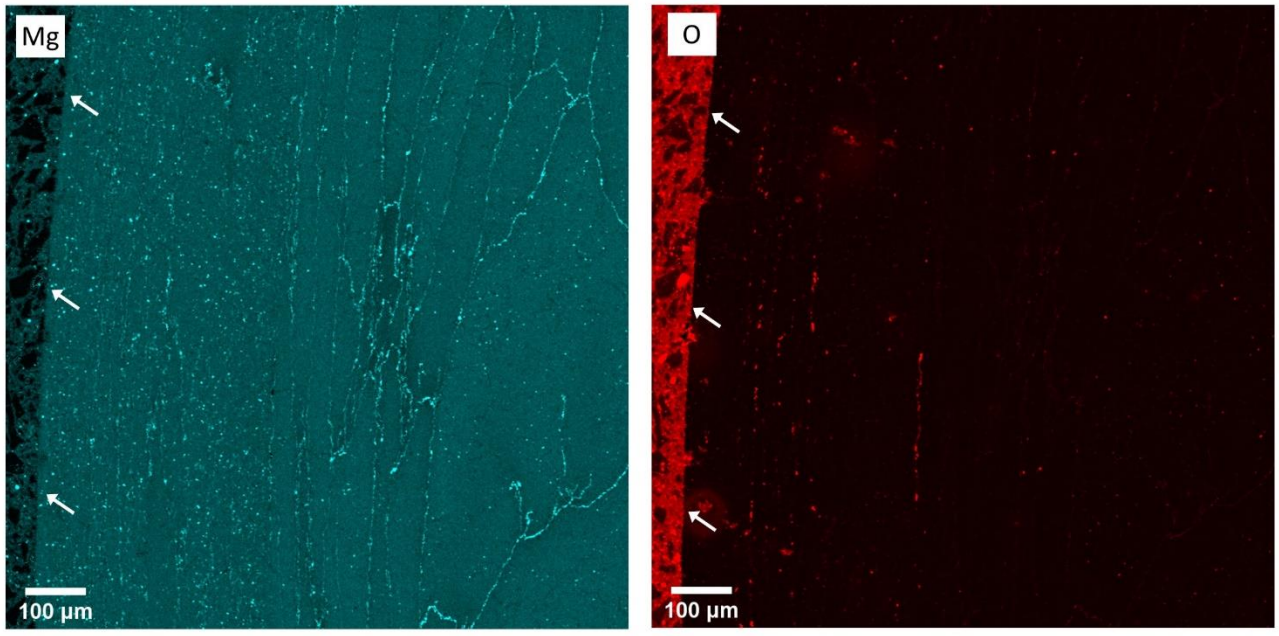

Fig. S 2 : Mg and O elemental maps obtained by EPMA of the solid-state recycled aluminium alloy (AA-chips-HE). The observed area is perpendicular to the extrusion direction and close from the periphery of the extrudate cylinder (as indicated by white arrows).

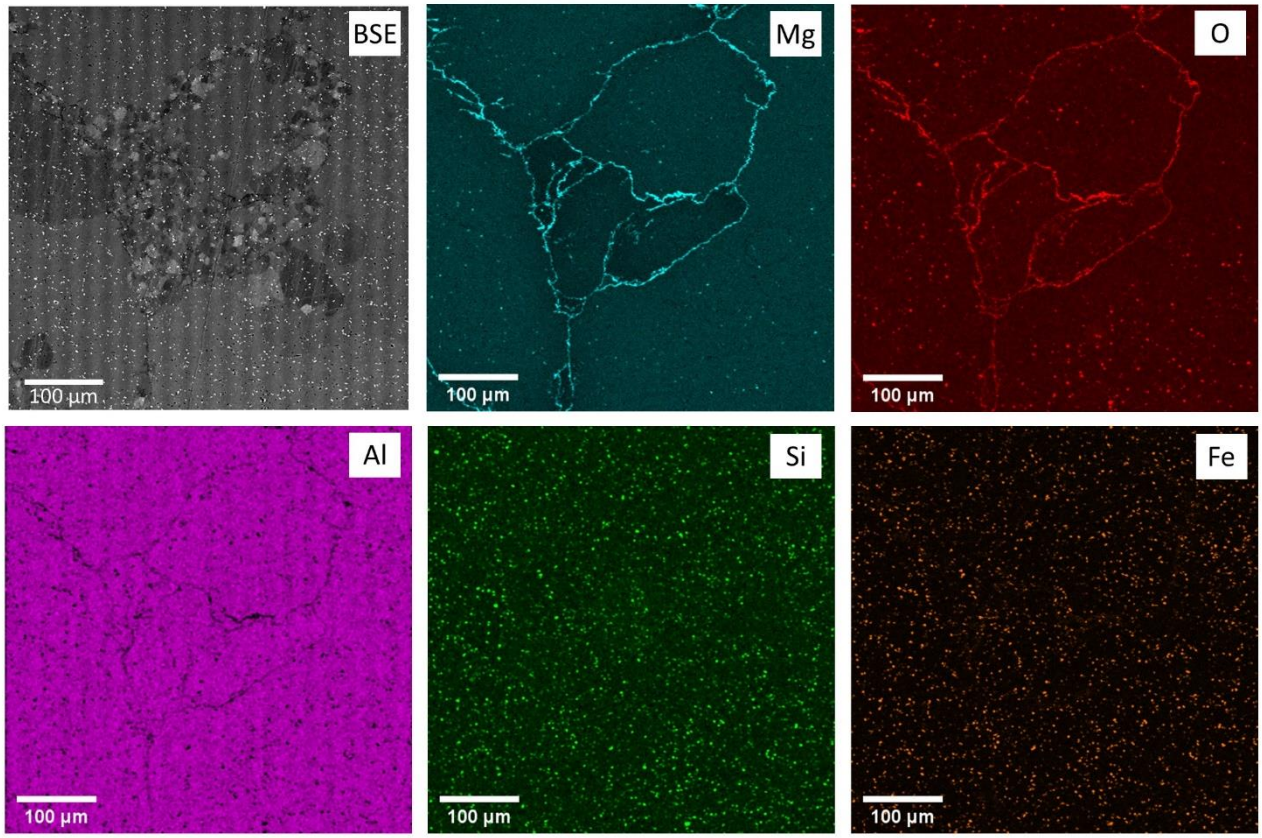

Fig. S 3 : Back-scattered electron (BSE) and elemental maps obtained by EPMA of the solid-state recycled aluminium alloy (AA-chips-HE) in the middle of the cylinder. The scale bar is the same on all maps.

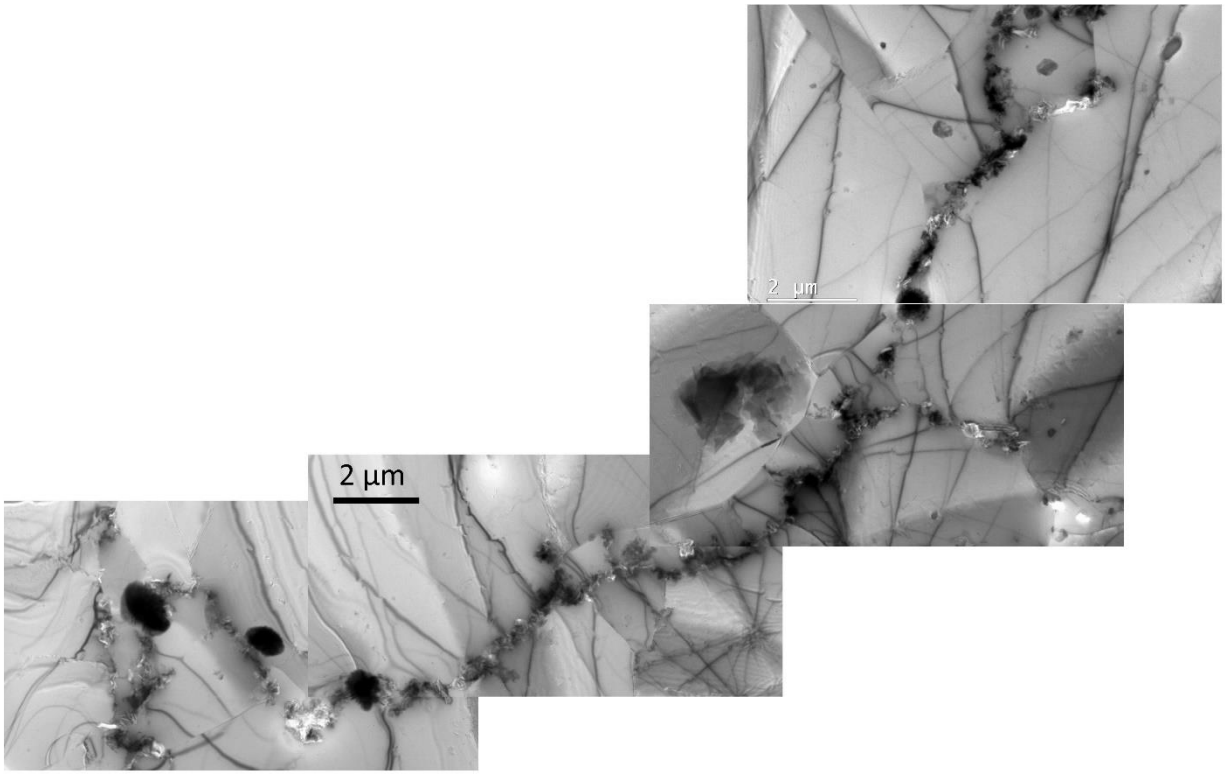

Fig. S 4 : TEM characterization of the solid-state recycled aluminium alloy (AA-chips-HE). Juxtaposition of several XX images following a PCB.

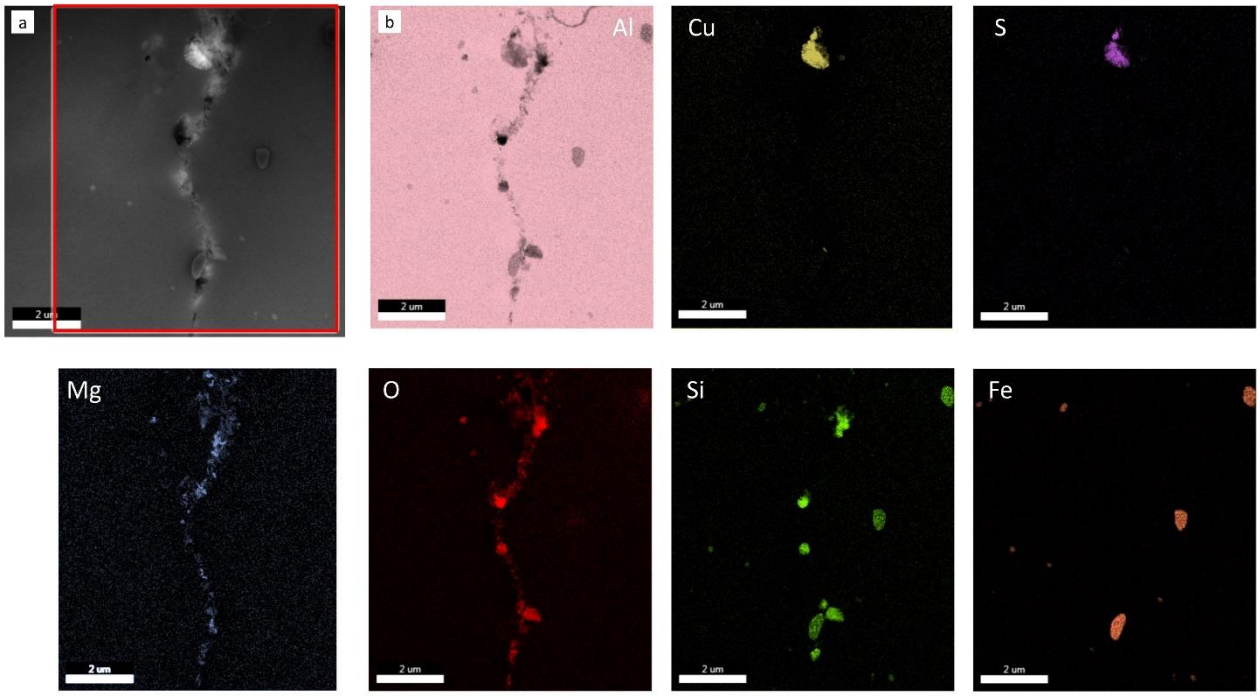

Fig. S 5 : TEM characterization of the solid-state recycled aluminium alloy (AA-chips-HE). (a) Bright field image. (b) EDS mapping of the area from (a) delimited by the red rectangle. The scale bar is of 2 µm for all images.

7.2. Data and formula for calculations

Table S 1 : Material data used for oxide layer thickness calculations based on XPS spectra.

Name (units)	Symbol	Values
Density (g.cm^{-3})	$\rho_{pure\ Al}$	2.7
	$\rho_{pure\ Al_2O_3}$	3.95
	$\rho_{pure\ MgO}$	3.58
Number density of element X in phase Y (mol.cm^{-3})	$D_{Al}^{pure\ Al}$	0.1
	$D_{Al}^{Al_2O_3}$	0.077
	D_{Mg}^{MgO}	0.0898
Transmission [28]	T_{Al}	3381
	T_{Mg}	3349
Cross-section of photo-ionization [28]	σ_{Al}	0.537
	σ_{Mg}	0.3335
Inelastic mean free path (IMFP) of element X in the phase Y (Å) [40]	$\lambda_{Al}^{pure\ Al}$	31,04
	$\lambda_{Al}^{Al_2O_3}$	32,8
	λ_{Al}^{MgO}	28,3

	λ_{Mg}^{MgO}	6,95

Calculation of number densities

$$D_{Al}^{pure\ Al} = \frac{\rho_{Al}}{M_{Al}}$$

$$D_{Al}^{Al2O3} = \frac{2}{2 * M_{Al} + 3 * M_O} * \rho_{Al2O3}$$

$$D_{Mg}^{MgO} = \frac{1}{M_{Mg} + M_O} * \rho_{MgO}$$

Where M_X is the atomic mass of element X

Calculation of the average weight oxygen concentration $[O]_{wt}$ in chips:

$$[O]_{wt} = \frac{m_O}{m_{Al}} = \frac{m_{ox} * f_{O,ox}}{m_{Al}}$$

Where: m is the mass, 'ox' and 'Al' subscripts refer respectively to oxide and aluminium alloy, and $f_{O,ox}$ is the molar fraction of oxygen in the oxide. Here the hypothesis is made that all O is contained in oxides. In other words, O in solid solution in aluminium is neglected.

$$[O]_{wt} = \frac{\rho_{ox} * V_{ox} * f_{O,ox}}{\rho_{Al} * V_{Al}}$$

Where ρ, S and V are respectively the density, the surface and the volume.

$$[O]_{wt} = \frac{\rho_{ox} \cdot f_{O,ox} \cdot e_{ox} \cdot S_{ox}}{\rho_{Al} \cdot V_{Al}}$$

The thickness e is introduced because it is an available experimental data. This is Eq. (7), which was used in the section 4.

$$f_{O,Al2O3} = \frac{3 * M_O}{2 * M_{Al} + 3 * M_O}$$

$$f_{O,MgO} = \frac{M_O}{M_{Mg} + M_O}$$

Where M_X is the atomic mass of element X

Calculation of the fraction of the chip oxide layer which grows during extrusion f_{growth} (in %)

The volume of oxides in the extrudates is equal to the oxides which have grown to reach a thickness $e_{ox,ext}$ of 290 nm as measured by TEM and the oxides that were already present on the chips and whose thickness e_{ox} remains constant (ie : 20 nm as measured by XPS).

$$V_{ox,ext} = S_{ox} * e_{ox} * \left(1 - f_{growth}\right) + S_{ox} * e_{ox,ext} * f_{growth}$$

Where 'ext' subscript refers to extrudate samples (AA-chips-HE).

Then, it can be inserted in Eq. (7) to express f_{growth} with available experimental data

$$f_{growth} = \frac{1}{e_{ox,ext} - e_{ox}} * \left(\frac{[O]_{wt}}{f_{O,ox}} * \frac{\rho_{Al}}{\rho_{ox}} * \frac{1}{\frac{S_{ox}}{V_{total}}} - e_{ox}\right) \quad \text{Eq. (8)}$$

This equation was used in the section 4. It is mentioned that, when neglecting the oxides which do not grow during extrusion, a value of 18.9 % is found for f_{growth}, very close of the result of 20 % without this approximation.

8. References

[1] Saevarsdottir, G., Kvande, H., and Welch, B.J., *Aluminum Production in the Times of Climate Change: The Global Challenge to Reduce the Carbon Footprint and Prevent Carbon Leakage.* JOM, **2020**. 72(1): p. 296-308.

[2] Capuzzi, S. and Timelli, G., *Preparation and Melting of Scrap in Aluminum Recycling: A Review.* Metals, **2018**. 8(4).

[3] Gronostajski, J., Marciniak, H., and Matuszak, A., *New methods of aluminium and aluminium-alloy chips recycling.* Journal of Materials Processing Technology, **2000**. 106(1-3): p. 34-39.

[4] Gronostajski, J.Z., Kaczmar, J.W., Marciniak, H., and Matuszak, A., *Direct recycling of aluminium chips into extruded products.* Journal of Materials Processing Technology, **1997**. 64(1): p. 149-156.

[5] Tekkaya, A.E., Schikorra, M., Becker, D., Biermann, D., Hammer, N., and Pantke, K., *Hot profile extrusion of AA-6060 aluminum chips.* Journal of Materials Processing Technology, **2009**. 209(7): p. 3343-3350.

[6] Misiolek, W.Z. and Kelly, R.M., *Extrusion of aluminum alloys*, in *ASM Handbook, Metalworking: Bulk Forming*. 2005, ASM International. p. 522-527.

[7] Duflou, J.R., Tekkaya, A.E., Haase, M., Welo, T., Vanmeensel, K., Kellens, K., Dewulf, W., and Paraskevas, D., *Environmental assessment of solid state recycling routes for aluminium alloys: Can solid state processes significantly reduce the environmental impact of aluminium recycling?* CIRP Annals, **2015**. 64(1): p. 37-40.

[8] Wideroe, F. and Welo, T., *Using contrast material techniques to determine metal flow in screw extrusion of aluminium.* Journal of Materials Processing Technology, **2013**. 213(7): p. 1007-1018.

[9] Tang, W. and Reynolds, A.P., *Production of wire via friction extrusion of aluminum alloy machining chips.* Journal of Materials Processing Technology, **2010**. 210(15): p. 2231-2237.

[10] Paraskevas, D., Vanmeensel, K., Vleugels, J., Dewulf, W., Deng, Y.L., and Duflou, J.R., *Spark Plasma Sintering As a Solid-State Recycling Technique: The Case of Aluminum Alloy Scrap Consolidation.* Materials, **2014**. 7(8): p. 5664-5687.

[11] Wan, B., Chen, W., Lu, T., Liu, F., Jiang, Z., and Mao, M., *Review of solid state recycling of aluminum chips.* Resources, Conservation and Recycling, **2017**. 125: p. 37-47.

[12] Stern, M., *Method for treating aluminum or aluminum alloy scrap* **1942**.

[13] Haase, M. and Tekkaya, A.E., *Recycling of Aluminum Chips by Hot Extrusion with Subsequent Cold Extrusion.* Procedia Engineering, **2014**. 81: p. 652-657.

[14] Güley, V., Güzel, A., Jäger, A., Ben Khalifa, N., Tekkaya, A.E., and Misiolek, W.Z., *Effect of die design on the welding quality during solid state recycling of AA6060 chips by hot extrusion.* Materials Science and Engineering: A, **2013**. 574: p. 163-175.

[15] Güley, V., Ben Khalifa, N., and Tekkaya, A.E. *The Effect of Extrusion Ratio and Material Flow on the Mechanical Properties of Aluminum Profiles Solid State Re-cycled from 6060 Aluminum Alloy Chips*. in *AIP Conference Proceedings: The 14th International ESAFORM Conference on Material Forming*. **Year**. Belfast.

[16] Wu, S., Ji, Z., and Zhang, T., *Microstructure and mechanical properties of AZ31B magnesium alloy recycled by solid-state process from different size chips.* Journal of Materials Processing Technology, **2009**. 209(12): p. 5319-5324.

[17] Wagiman, A., Mustapa, M.S., Asmawi, R., Shamsudin, S., Lajis, M.A., and Mutoh, Y., *A review on direct hot extrusion technique in recycling of aluminium chips.* International Journal of Advanced Manufacturing Technology, **2020**. 106(1-2): p. 641-653.

[18] McDonald, D.T., Luo, P., Palanisamy, S., Dargusch, M.S., and Xia, K., *Ti-6Al-4V Recycled From Machining Chips by Equal Channel Angular Pressing*, in *Powder Metallurgy of Titanium: Powder Processing, Consolidation and Metallurgy of Titanium*, M. Qian, Editor. 2012, Trans Tech Publications Ltd: Durnten-Zurich. p. 295-+.

[19] Zhang, W., Bay, N., and Wanheim, T., *Influence of hydrostatic Pressure in Cold-Pressure Welding.* CIRP Annals, **1992**. 41(1): p. 293-297.

[20] Cooper, D.R. and Allwood, J.M., *The influence of deformation conditions in solid-state aluminium welding processes on the resulting weld strength.* Journal of Materials Processing Technology, **2014**. 214(11): p. 2576-2592.

[21] Kolpak, F., Schulze, A., Dahnke, C., and Tekkaya, A.E., *Predicting weld-quality in direct hot extrusion of aluminium chips.* Journal of Materials Processing Technology, **2019**. 274: p. 116294.

[22] Schulze, A., Hering, O., and Erman Tekkaya, A. *Welding of Aluminium in Chip Extrusion*. in *Forming the Future*. **Year**. Cham: Springer International Publishing.

[23] Haase, M. and Tekkaya, A.E., *Cold extrusion of hot extruded aluminum chips.* Journal of Materials Processing Technology, **2015**. 217: p. 356-367.

[24] Schulze, A., Hering, O., and Tekkaya, A.E., *Production and Subsequent Forming of Chip-Based Aluminium Sheets Without Remelting.* International Journal of Precision Engineering and Manufacturing-Green Technology, **2022**. 9(4): p. 1035-1048.

[25] Olefjord, I., Mathieu, H.J., and Marcus, P., *Intercomparison of surface analysis of thin aluminium oxide films.* Surface and Interface Analysis, **1990**. 15(11): p. 681-692.

[26] Hyde, J.M., DaCosta, G., Hatzoglou, C., Weekes, H., Radiguet, B., Styman, P.D., Vurpillot, F., Pareige, C., Etienne, A., Bonny, G., Castin, N., Malerba, L., and Pareige, P., *Analysis of Radiation Damage in Light Water Reactors: Comparison of Cluster Analysis Methods for the Analysis of Atom Probe Data.* Microscopy and Microanalysis, **2017**. 23(2): p. 366-375.

[27] Wriedt, H.A., *The Al-O (Aluminum-Oxygen) system.* Bulletin of Alloy Phase Diagrams, **1985**. 6(6): p. 548-553.

[28] Liu, M., Zanna, S., Ardelean, H., Frateur, I., Schmutz, P., Song, G., Atrens, A., and Marcus, P., *A first quantitative XPS study of the surface films formed, by exposure to water, on Mg and on the Mg–Al intermetallics: Al3Mg2 and Mg17Al12.* Corrosion Science, **2009**. 51(5): p. 1115-1127.

[29] Cornette, P., Zanna, S., Seyeux, A., Costa, D., and Marcus, P., *The native oxide film on a model aluminium-copper alloy studied by XPS and ToF-SIMS.* Corrosion Science, **2020**. 174: p. 108837.

[30] *Ellingham Diagrams.* Cambridge University, **Visited on 03/03/2023)**. https://www.doitpoms.ac.uk/tlplib/ellingham_diagrams/printall.php.

[31] Trunov, M.A., Schoenitz, M., and Dreizin, E.L., *Effect of polymorphic phase transformations in alumina layer on ignition of aluminium particles.* Combustion Theory and Modelling, **2006**. 10(4): p. 603-623.

[32] Nylund, A., Mizuno, K., and Olefjord, I., *Influence of Mg and Si on the Oxidation of Aluminum.* Oxidation of Metals, **1998**. 50(3): p. 309-325.

[33] Holub, K.J. and Matienzo, L.J., *MAGNESIUM DIFFUSION IN SEVERAL ALUMINUM-ALLOYS.* Applied Surface Science, **1981**. 9(1-4): p. 22-38.

[34] De Geuser, F., Lefebvre, W., and Blavette, D., *3D atom probe study of solute atoms clustering during natural ageing and pre-ageing of an Al-Mg-Si alloy.* Philosophical Magazine Letters, **2006**. 86(4): p. 227-234.

[35] Engler, O., Marioara, C.D., Aruga, Y., Kozuka, M., and Myhr, O.R., *Effect of natural ageing or pre-ageing on the evolution of precipitate structure and strength during age hardening of Al-Mg-Si alloy AA 6016.*

Materials Science and Engineering a-Structural Materials Properties Microstructure and Processing, **2019**. 759: p. 520-529.

[36] Marioara, C.D., Andersen, S.J., Jansen, J., and Zandbergen, H.W., *Atomic model for GP-zones in a 6082 Al-Mg-Si system.* Acta Materialia, **2001**. 49(2): p. 321-328.

[37] Tylecote, R.F., *The Solid Phase Welding of Metals*. 1968, London: Edward Arnold.

[38] Toualbi, L., Cayron, C., Olier, P., Malaplate, J., Praud, M., Mathon, M.H., Bossu, D., Rouesne, E., Montani, A., Loge, R., and de Carlan, Y., *Assessment of a new fabrication route for Fe-9Cr-1W ODS cladding tubes.* Journal of Nuclear Materials, **2012**. 428(1-3): p. 47-53.

[39] Misiolek, W.Z. and Kelly, R.M., *Extrusion of Aluminum Alloys*, in *Metalworking: Bulk Forming*, S.L. Semiatin, Editor. 2005, ASM International. p. 0.

[40] Tanuma, S., Powell, C.J., and Penn, D.R., *CALCULATIONS OF ELECTRON INELASTIC MEAN FREE PATHS .2. DATA FOR 27 ELEMENTS OVER THE 50-2000-EV RANGE.* Surface and Interface Analysis, **1991**. 17(13): p. 911-926.